



1 **Moment magnitude estimates for Central Anatolian earthquakes using coda waves**

2

3 Tuna Eken<sup>1</sup>

4

5 <sup>1</sup>*Department of Geophysical Engineering, the Faculty of Mines, Istanbul Technical*

6 *University, 34469 Maslak, Sarıyer, Istanbul, Turkey*

7

8 *Abstract*

9 Proper estimate of moment magnitude that is a physical measure of the energy released at  
10 earthquake source is essential for better seismic hazard assessments in tectonically active  
11 regions. Here a coda wave modeling approach that enables the source displacement spectrum  
12 modeling of examined event was used to estimate moment magnitude of central Anatolia  
13 earthquakes. To achieve this aim, three component waveforms of local earthquakes with  
14 magnitudes  $2.0 \leq M_L \leq 5.2$  recorded at 72 seismic stations which have been operated  
15 between 2013 and 2015 within the framework of the CD-CAT passive seismic experiment.  
16 An inversion on the coda wave traces of each selected single event in our database was  
17 performed in five different frequency bands between 0.75 and 12 Hz. Our resultant moment  
18 magnitudes ( $M_W$ -coda) exhibit a good agreement with routinely reported local magnitude  
19 ( $M_L$ ) estimates for study area. Finally, we present an empirical relation between  $M_W$ -coda and  
20  $M_L$  for central Anatolian earthquakes.

21

22 Keyword(s): Coda waves modelling, seismic moment, moment magnitude, Radiative Transfer  
23 Theory

24

25



26 *1. Introduction*

27 The robust and stable knowledge of source properties (e.g. moment magnitude estimates) is  
28 crucial in seismically active countries such as Turkey for a better evaluation of seismic hazard  
29 potential as this highly depends on establishment of reliable seismicity catalogs. Moreover,  
30 accurate information on source parameters could be important when developing regional  
31 attenuation properties.

32

33 Conventional type of magnitude scales ( $M_L$ ,  $m_b$ ,  $M_S$ ) as the result of empirically derived using  
34 direct wave analyses can be biased due to various effects such as source radiation pattern,  
35 directivity, and heterogeneities along the path since they may cause drastic changes in direct  
36 wave amplitude measurements (e.g., Favreau and Archuleta, 2003). Instead several early  
37 studies depending on the analysis of local and/or regional coda envelopes have indicated that  
38 coda wave amplitudes are significantly less variable by a factor of 3-to-5 compared to direct  
39 wave amplitudes (e.g., Mayeda and Walter, 1996; Mayeda et al., 2003; Eken et al., 2004;  
40 Malagnini et al., 2004; Gök et al., 2016). In fact local or regional coda waves that are usually  
41 considered to be generally to be composed of scattered waves and can be simply explained by  
42 that sample the single scattering model of Aki (1969) have been proven to be virtually  
43 insensitive to any source radiation pattern effect in contrast to direct waves because of the  
44 volume averaging property of the coda waves sampling the entire focal sphere (e.g., Aki and  
45 Chouet, 1975; Rautian and Khalturin, 1978). In Sato and Fehler (1998) and Sato et al. (2012)  
46 an extensive review study on the theoretical background of coda generation and advances of  
47 empirical observations and modelling efforts can be found in details.

48

49 There have been several approaches used for extracting information on earthquake source size  
50 via coda wave analyses. These approaches can be mainly divided into two groups. The first



51 group of studies employs coda normalization strategy in which measurements require a  
52 correction for seismic attenuation parameters (e.g. intrinsic and scattering) that can be  
53 described by some empirical quality factors. To calibrate final source properties reference  
54 events are used to adjust measurements with respect to each other. For forward generation of  
55 synthetic coda envelopes, either single-backscattering or more advanced multiple-  
56 backscattering approximation are used. An example to this group is an empirical method  
57 originally developed by Mayeda et al. (2003) to investigate seismic source parameters such as  
58 energy, moment, and apparent stress drop in the western United States and in Middle East.  
59 They corrected observed coda envelopes for various influences, for instance, path effect, S-to-  
60 coda transfer function, site effect, and any distance-dependent changes in coda envelope  
61 shape. Empirical coda envelope method have been successfully applied to different regions  
62 with complicated tectonics such as northern Italy (e.g. Morasca et al., 2008), Turkey and  
63 Middle East (e.g. Eken et al., 2004; Gök et al. 2016); or Korean Peninsula (e.g. Yoo et al.,  
64 2013).

65

66 Second type of approach is a joint inversion technique that is based on a simultaneous  
67 optimization of source, path, and site specific terms via synthetic and observed coda envelope  
68 fitting within a selected time window including observed coda and direct-S wave parts. In this  
69 approach, the Radiative Transfer Theory (RTT) is employed for analytic expression of  
70 synthetic coda wave envelopes. The method that does not rely on coda normalization strategy  
71 was originally developed by Sens-Schönfelder and Wegler (2006) and successfully tested on  
72 local and regional earthquakes ( $4 \leq M_I \leq 6$ ) detected by the German Regional Seismic  
73 Network. Further it has been applied to investigate source and frequency dependent  
74 attenuation properties of different geological settings, i.e., Upper Rhine Graben and Molasse  
75 Basin regions in Germany and western Bohemia/Vogtland in Czechia (Eulenfeld and Wegler,



76 2016); entire United States (2017); central and western North Anatolian Fault Zone (Gaebler  
77 et al., 2018; Izgi et al., 2018). A more realistic earth model in which anisotropic scattering  
78 conditions were earlier considered by Gusev and Abubakirov (1987) yielded peak broadening  
79 effects of the direct seismic wave arrivals. This approach later was used in previous studies  
80 (e.g. Zeng, 1993; Przybilla and Korn, 2008; Gaebler et al., 2015) that dealt with propagation  
81 of P-wave elastic energy and the effect of conversion between P- and S-wave energies.

82

83 In the current work I present estimated source spectra as an output of a joint inversion of S-  
84 and coda waves parts of local earthquake waveforms 487 local earthquakes with magnitudes  
85  $2.0 < ML < 4.5$  detected in central Anatolia for their source parameters. The approach used  
86 here employs isotropic acoustic RTT approach for forward calculation of synthetic coda  
87 envelopes. Gaebler et al. (2015) has observed that modeling results from isotropic scattering  
88 were almost comparable with those inferred from relatively more complex elastic RTT  
89 simulations with anisotropic scattering conditions. The use of a joint inversion technique is  
90 advantageous since it is insensitive to any potential bias, which could be introduced by  
91 external information, i.e., source properties of a reference that is obtained separately from  
92 other methods for calibration. This is mainly because of the fact that we utilize an analytical  
93 expression of physical model involving source, and path related parameters to describe the  
94 scattering process. Moreover the type of optimization during joint inversion enables the  
95 estimates for source parameters of relatively small sized events compared to the one used in  
96 coda-normalization methods.

97

98

99

100



101        2. *Regional Setting and Data*

102 Present tectonic setting of Anatolia and surrounding regions have been mainly outcome of the  
103 northward converging movements among Africa, Arab, and Eurasian plates. To the west  
104 subducting African plate with a slab roll-back dynamics beneath Anatolia along Hellenic  
105 Trench has led to back-arc extension in the Aegean and western Anatolia while compressional  
106 deformation to the east around the Bitlis–Zagros suture was explained by collisional tectonics  
107 (e.g. Taymaz et al., 1990; Bozkurt, 2001). Westward extrusion of Anatolian plate controlled  
108 by these plate motions, in consequence, has been accommodated through two conjugate  
109 strike-slip fault zones separating the Anatolian and Arabian from Eurasian plates: 1600 km  
110 long east-west striking transform plate boundary, North Anatolian fault zone (NAFZ), and  
111 northeast-southwest–striking East Anatolian fault zone (EAFZ) (Fig. 1). These neotectonic  
112 features could have easily traced the weakness zones along the boundaries of amalgamated  
113 continental fragments that have developed following the closure of Tethys Ocean (Şengör et  
114 al., 2005).

115

116 Central Anatolia is located between extensional regime to the west due to the subduction and  
117 compressional regime tectonics to the east due to the collisional tectonics. The major fault  
118 zone in the region, the Central Anatolian Fault Zone (CAFZ) (Fig. 2), which primarily  
119 represents a transtensional fault structure with small amount of left-lateral offset during the  
120 Miocene (e.g. Koçyiğit and Beyhan, 1998), can be considered as a boundary between the  
121 carbonate nappes of the Anatolide-Tauride block from the highly deformed and  
122 metamorphosed rocks in the Kırşehir block. However recent studies that have reported  
123 significant lateral variations in seismic wave speeds (e.g. Fichtner et al., 2013a,b; Delph et al.,  
124 2015) and Bouguer gravity (Ateş et al., 1999) across the fault implied that a progressive  
125 relative movement along the faults would result in sharp difference in crust and mantle



126 structures. New findings on structural, geomorphic, and geochronologic data collected from  
127 several segments along the CAFZ were interpreted that the transtensional type deformation  
128 has reactivated paleotectonic structures and finally accommodated E-W extension due to the  
129 westward extrusion of Anatolia (Higgins et al., 2015). To the northwest of the CAFZ, Tuz  
130 Gölü Fault Zone (TGFZ) (Fig. 2), which is characterized by a right-lateral strike slip motion  
131 with a significant oblique-slip normal component, appears to be collocated with Tuz Gölü  
132 Basin sedimentary deposits as well as crystalline rocks within Kırşehir Block (e.g. Çemen et  
133 al., 1999; Bozkurt et al., 2001; Taymaz et al., 2004). Present day crustal deformation and state  
134 of stress related to the TGFZ have been reported in Çubuk et al. (2014) via observed  
135 earthquake cluster activity reaching depths of 5-6 km with magnitudes up to  $M_L 5.6$  in the  
136 Bala region (between 2005 and 2007) located at the north of the TGFZ (Çubuk et al., 2014).

137

138 At the southwest tip of the study region, the EAFZ generates large seismic activity that can be  
139 identified rather complicated seismotectonic setting: predominantly left-lateral strike-slip  
140 motion correlated well with the regional deformation pattern but also existing local clusters of  
141 thrust and normal faulting events on NS- and EW-trending subsidiary faults, respectively  
142 (Bulut et al., 2012). Such complicated behavior explains kinematic models of the shear  
143 deformation zone evolution. This active left-lateral fault zone since the late Miocene–Pliocene  
144 exhibits ~20 km-wide shear deformation zone with an annual 6-10 mm/yr slip rate. It  
145 connects to the NAFZ at the Karlıova Triple Junction (Bozkurt, 2001) and to the south splits  
146 into various segments nearby the Adana Basin (Kaymakci et al., 2006) (Fig. 2). Toward the  
147 south, the EAFZ reaches the Dead Sea Fault Zone (DSFZ) that has a key role in  
148 accommodating northward relative motions of Arabian and African Plates with respect to  
149 Eurasia.



150 The present work utilizes three-component waveforms of local seismic activity detected at 72  
151 broadband seismic stations (Fig. 2) that have been operated for 2 years between 2013 and  
152 2015 within the framework of a temporary passive seismic experiment, the Continental  
153 Dynamics–Central Anatolian Tectonics (CD-CAT) (Portner et al., 2018). We benefit from  
154 revisited standard earthquake catalogue information (publicly available at  
155 <http://www.koeri.boun.edu.tr>) to extract waveform data for a total of 2231 examined events  
156 with station-event pair distance less than 120 km and focal depths less than 10 km. Most of  
157 the detected seismic activity in the study area is associated to several fault zones in the region,  
158 i.e., the EAFZ, CAFZ, DSFZ, TGFZ, etc. Here we note that selection of only local  
159 earthquakes is to exclude possible biases, which may be introduced by Moho boundary  
160 guided Sn-waves while upper crustal earthquakes are preferred in this study to exclude effect  
161 of relatively large-scale heterogeneities on coda wave trains. Finally a visual inspection  
162 conducted over all waveforms to ensure high-quality waveforms reduces our event number to  
163 1193. Selected station and event distributions can be seen in Figure 2.

164

165 Observed waveforms were prepared at 5 different frequency bands with central frequencies at  
166 0.75, 1.5, 3.0, 6.0, 12.0 Hz via a Butterworth band-pass filtering process. In the next step, we  
167 applied Hilbert transform to filtered waveform data in order to obtain the total energy  
168 envelopes. An average crustal velocity model was used to predict P and S wave onsets on  
169 envelopes and then based on this information: (i) the noise level prior to the P-wave onset was  
170 eliminated (ii) S-wave window was determined starting at 3s prior to and 7 s afterwards S-  
171 wave onset as this allowed to include all direct S-wave energy, (iii) starting at the end of the  
172 S-wave window, a coda window of 100s at maximum was determined. Length of coda  
173 windows can be shorter when signal-to-noise ratio (SNR) is less than 2.5 or when the same



174 window consists of coda waves from two earthquakes, which can give rise to a decline in the  
175 envelope. We omit the earthquakes with less than 10 s of coda length from our database.

176

### 177 3. Method

178 We adopted an inversion procedure that was originally developed by Sens-Schönfelder and  
179 Wegler (2006) and later modified by Eulenfeld and Wegler (2016). The forward part, which  
180 involves calculation of energy density for a specific frequency band caused by an isotropic  
181 source, is expressed in Sens-Schönfelder and Wegler (2006) as follows:

$$182 \quad E_{mod}(t, r) = WR(r)G(t, r, g)e^{-bt} \quad (1)$$

183

184 where  $G(t, r, g)$  represents Green's function that includes scattered wave field as well as  
185 direct wave.  $W$  gives source term and it is frequency dependent.  $R(r)$  indicates the energy site  
186 amplification factor and  $b$  is intrinsic attenuation parameter.

187 Possible discrepancy between predicted and observed energy densities for each event at each  
188 station with  $N_{ij}$  time samples (index  $k$ ) in a specific frequency band can be minimized using:

189

$$190 \quad \epsilon(g) = \sum_{i,j,k}^{N_s, N_s, N_{ij}} (\ln E_{ijk}^{obs} - \ln E_{ijk}^{mod}(g))^2 \quad (2)$$

191

192 Here, the number of stations (index  $i$ ) and events (index  $j$ ) are shown by  $N_s$  and  $N_E$ ,  
193 respectively. Optimization of  $g$  will be achieved when

194

$$195 \quad \ln E_{ijk}^{obs} = \ln E_{ijk}^{mod} \quad (3) \quad \text{or}$$

196

$$197 \quad \ln E_{ijk}^{obs} = \ln G t_{ijk}, r_{ijk}, g + \ln R_i + \ln W_j - b t_{ijk} \quad (4)$$



198 Equation 4 simply define an overdetermined inversion problem with  $\sum_{i,j} N_{ij}$  number equation  
199 systems and with  $N_S + N_E + 1$  variables and thus  $b$ ,  $R_i$ , and  $W_j$  can be solved via a least-  
200 squares technique.  $\epsilon(g)$  can be defined as sum over the squared residuals of the solution.

201 Eulenfeld and Wegler (2016) present a simple recipe to perform inversion:

202 (i) Calculate Green's functions through the analytic approximation of the solution for 3-D  
203 isotropic radiative transfer (e.g. Paasschens 1997; Sens-Schönfelder and Wegler, 2006) by  
204 using fixed scattering parameters and minimize equation 4 to solve for  $b$ ,  $R_i$ , and  $W_j$  via a  
205 weighted least-squares approach.

206 (ii) Calculate  $\epsilon(g)$  using equation 2.

207 (iii) Repeat (i) and (ii) by selecting different  $g$  to find the optimal parameters  $g$ ,  $b$ ,  $R_i$  and  $W_j$   
208 that finally minimize the error function  $\epsilon$ .

209 In Fig. 3 an example for the minimization process that was applied at five different frequency  
210 band is displayed for one selected event at recorded stations of the CD-CAT project.

211 Minimization described above for different frequencies will yield unknown spectral source  
212 energy term,  $W_j$  as well as site response,  $R_i$  and attenuation parameters,  $b$ , and  $g$ . The present  
213 study deals with frequency dependency of  $W_j$  since this information can be later useful to  
214 obtain source displacement spectrum and thus seismic moment and moment magnitudes of  
215 analyzed earthquakes using the formula of the  $S$ -wave source displacement spectrum for a  
216 double-couple source in the far-field, which is given by Sato et al. (2012):

217 
$$\omega M(f) = \sqrt{\frac{5\rho_0 v_0^5 W}{2\pi f^2}} \quad (5)$$

218



219 The relation between the obtained source displacement spectrum and seismic moment value  
220 was earlier described in Abercrombie (1995) by:

$$221 \quad \omega M(f) = M_0 \left(1 + \left(\frac{f}{f_c}\right)^{\gamma n}\right)^{-\frac{1}{\gamma}} \quad (6)$$

222 where  $n$  is related to the high-frequency fall-off and  $\gamma$  is known as shape parameter that  
223 controls the sharpness of spectrum at corner frequency between the constant level  $M_0$  (low  
224 frequency part) and the fall-off with  $f^{-n}$  (high frequency part). Taking logarithm of equation 6  
225 gives:

$$226 \quad \ln \omega M(f) = \ln M_0 - \frac{1}{\gamma} \ln \left(1 + \left(\frac{f}{f_c}\right)^{\gamma n}\right) \quad (7)$$

227  
228  
229 Eq.7 describes an optimization problem of which data forms observed source displacement  
230 spectrum and four source parameters,  $M_0$ ,  $\gamma$ ,  $n$ , and  $f_c$  are the unknown model parameters that  
231 can be resolved in a simultaneous least-squares inversion of the equation 7. Finally moment  
232 magnitude,  $M_w$  can be calculated from modeled source parameters, seismic moment,  $M_0$   
233 using a formula given by Hanks and Kanamori (1979):

$$234 \quad M_w = \frac{2}{3} \log_{10} M_0 - 6.07 \quad (8)$$

#### 235 236 237 *4. Results and Discussions*

##### 238 *4.1 Coda wave source spectra*

239 Figure 4 displays observed values of source spectra established by inserting inverted spectral  
240 source energy term  $W$  at each frequency in Eq. 5 for all analyzed events. Each curve in this  
241 figure represents model spectrum estimate based on inversion procedure described in previous



242 section. Modeled spectrum characteristics computed for 487 local earthquakes of which  
243 lateral distribution is presented in Figure 2 suggest, in general, that we were able to obtain  
244 typically expected source displacement spectrum with a flat region around the low frequency  
245 limit and decaying behaviour above a corner frequency.

246

247 Owing to the multiple-scattering process within small scale heterogeneities that makes coda  
248 waves gain an averaging nature, the variation in coda amplitudes due to differences source  
249 radiation pattern and path effect are reduced (Walter et al., 1995; Mayeda et al., 2003).  
250 Eulenfeld and Wegler (2016) found that radiation pattern would have only a minor influence  
251 on the S-wave coda while it might disturb attenuation models inferred from the direct S-wave  
252 analyses unless the station distribution relative to the earthquakes indicates a good azimuthal  
253 coverage. A peak-like source function assumption for small earthquakes that are utilized in  
254 the present work was earlier proven to be adequate in early application of the coda-wave  
255 fitting studies (e.g. Sens-Schönfelder and Wegler, 2006; Gaebler et al., 2015; and Eulenfeld  
256 and Wegler, 2016).

257

258 Conventional approaches (e.g. Abercrombie, 1995; Kwiatek et al., 2011) to estimate source  
259 parameters such as corner frequency, seismic moment, high-frequency fall-off through fitting  
260 of observed displacement spectra observed at a given station in an inversion scheme could be  
261 misleading since these methods usually: (i) assume a constant value of attenuation effect (no  
262 frequency variation) defined by a factor  $\exp(-\pi f t Q^{-1})$  over the spectrum, (ii) and assume  
263 omega-square model with a constant high-frequency fall-off parameter,  $n=2$ . Following Sens-  
264 Schönfelder and Wegler (2006) and Eulenfeld and Wegler (2016), however, we estimate  
265 attenuation parameters (intrinsic and scattering) separately within a simultaneous inversion  
266 procedure in which high-frequency fall-off parameter varies. This is fairly consistent with



267 early studies (e.g. Ambeh and Fairhead, 1991; Eulenfeld and Wegler, 2016) where significant  
268 deviations from the omega square model ( $n > 3$ ) were reported implying that the omega-square  
269 model as a source model for small earthquakes must be reconsidered in its general  
270 acceptance. In our case, the smallest event was with  $M_{W-coda}$  larger than 2.0, thus we had no  
271 chance to make a similar comparison, however, high-frequency fall-off parameters varied  
272 from  $n=0.5$  to  $n=4$ . A notable observation in the distribution of  $n$  was  $n=2$  or  $n=2.5$  would be  
273 better explain earthquakes with  $M_{W-coda} > 4.0$  whereas the smaller magnitudes exhibited  
274 more scattered pattern of variation in  $n$ . Eulenfeld and Wegler (2016) claimed that the use of  
275 separate estimates of the attenuation or correction for path effect via empirically determined  
276 Green's function would be better strategy in order to invert station displacement spectra for  
277 source parameters. This is mainly because smaller earthquakes (with  $n > 2$ ), in particular,  
278 assuming omega-square model can distort the estimates of corner frequency and even seismic  
279 moment especially in regions where  $Q$  is strongly frequency dependent.

280

#### 281 *4.2 Coda wave –derived magnitude vs. $M_L$ catalogue magnitude*

282 A scatter plot between catalogue magnitudes based on local magnitudes ( $M_L$ ) and our coda-  
283 derived magnitudes ( $M_{W-coda}$ ) that are inferred from resultant frequency dependent source  
284 displacement spectra and thus seismic moment (e.g. Eq. 8) is shown in Fig. 6. Such  
285 comparison suggests an overall coherency between both types of magnitudes. This implies  
286 very simple model of a first-order approximation for S-wave scattering with isotropic acoustic  
287 radiative transfer approach can be efficient to link the amplitude and decaying character of  
288 coda wave envelopes to the seismic moment of the source.

289





290 A linear regression analyses performed between  $M_W$ -coda and  $M_L$  magnitudes (Fig. 5)  
291 resulted in an empirical formula that can be employed to convert local magnitudes into coda-  
292 derived moment magnitude calculation of local earthquakes in this region:

293

$$294 \quad M_{W-coda} = 1.1655 \pm 0.0337 \times M_L - 0.7085 \pm 0.0128 \quad (9)$$

295

296 Apparent move-out in Fig. 5 and Eq. 9, presumably stems from the use of different magnitude  
297 scales for comparison. The consistency between coda-derived moment magnitude and local  
298 magnitude scales for the earthquakes with  $M_W$ -coda > 3.0 indicates that our non-empirical  
299 approach successfully worked in this tectonically complex region. We observed similar type  
300 of consistency in early studies that investigate source properties of local and regional  
301 earthquakes based on empirical coda methods with simple 1-D radially symmetric path  
302 correction (e.g. Eken et al., 2004; Gök et al., 2016). Observable outliers in Figure 5, for the  
303 events with less than  $M_w$  3.5, however, can be attributed to the either possible biases on local  
304 magnitude values taken from the catalogue or small biases on our intrinsic ( $Q_i^{-1}$ ) and  
305 scattering ( $Q_s^{-1}$ ) attenuation terms. One another possible contribution to such mismatch might  
306 be associated to the influences of mode conversions between body and surface waves or  
307 surface-to-surface wave scattering (e.g. Wu & Aki 1985) that are not restricted to low  
308 frequencies (<1Hz) (Sens-Schönfelder and Wegler, 2006).

309

### 310 5. Conclusions

311 This study provides an independent solution for estimating seismic source parameters such as  
312 seismic moment and moment magnitude for local earthquakes in central Anatolia without  
313 requiring *a priori* information on reference events with waveform modelling results to be  
314 used for calibration or *a priori* information on attenuation for path effect corrections. In this



315 regard, the approach used here can be easy and useful tool for investigation of source  
316 properties of local events detected at temporal seismic networks. Moreover, seismic moment  
317 can be approximated via waveform modelling methods but due to the small-scale  
318 heterogeneities of the media that waves propagate, it is often a hard task to establish Green's  
319 function for small earthquake ( $M_L < 3.5$ ). An analytical expression of energy density Green's  
320 function in a statistical manner employed in the present work enables neglecting the  
321 interaction of the small-scale inhomogeneities with seismic waves as this can be practical for  
322 seismic moment calculations of small events that may pose source energy at high-frequency.  
323 It is noteworthy to mention that our isotropic scattering assumption does not consider  
324 anisotropic case, which could be valid for real media, but still provides a simple and effective  
325 tool to define the transport for the anisotropic case since the estimated scattering coefficient  
326 can be interpreted as transport scattering coefficient. An averaging over S-wave window  
327 enables to overcome biases caused by using unrealistic Green's function (Gaebler *et al.*  
328 2015). Since the present study mainly focuses on source properties of local earthquakes in the  
329 study area, scattering and intrinsic attenuation properties that are other products of our coda  
330 envelope fitting procedure will be examined in details within a future work. Finally, the  
331 empirical relation developed between  $M_W$ -coda and  $M_L$  will be a useful tool for quickly  
332 converting catalogue magnitudes to moment magnitudes for local earthquakes in the study  
333 area.

334

### 335 *Data and resources*

336 The python code used for carrying out the inverse modeling is available under the permissive  
337 MIT license and is distributed at <https://github.com/trichter/qopen>. We are grateful to the IRIS  
338 Data Management Center for maintaining, archiving and making the continuous broadband  
339 data used in this study open to the international scientific community.



340

341 *Acknowledgement*

342 The facilities of IRIS Data Services, and specifically the IRIS Data Management Center, were  
343 used for access to waveforms, related metadata, and/or derived products used in this study.

344 IRIS Data Services are funded through the Seismological Facilities for the Advancement of  
345 Geoscience and EarthScope (SAGE) Proposal of the National Science Foundation under  
346 Cooperative Agreement EAR-1261681. Data for the CD-CAT experiment  
347 ([https://doi.org/10.7914/SN/YB\\_2013](https://doi.org/10.7914/SN/YB_2013)) are available from the IRIS Data Management Center  
348 at <http://www.iris.edu/hq/>. Tuna Eken acknowledge financial support from Alexander von  
349 Humboldt Foundation (AvH) towards computational and peripherals resources.

350 *References*

351 Abercrombie, R.E.: Earthquake source scaling relationships from  $-1$  to  $5$  ML using  
352 seismograms recorded at 2.5-km depth, *J. geophys. Res.*, 100(B12), 24 015–24 036,  
353 1995.

354 Aki, K., and Chouet., B.: Origin of coda waves: Source, attenuation, and scattering effects, *J.*  
355 *Geophys. Res.* 80, 3322–3342, 1975.

356 Ates, A., Kearey, P., and Tufan, S.: New gravity and magnetic anomaly maps of Turkey:  
357 *Geophysical Journal International*, v. 136, p. 499–502, 1999.

358 Bozkurt, E.: Neotectonics of Turkey—A synthesis: *Geodynamica Acta*, v. 14, p. 3–30, 2001.

359 Bulut, F., Bohnhoff, M., Eken, T., Janssen, C., Kılıç, T., and Dresen, G.: The East Anatolian  
360 fault zone: Seismotectonic setting and spatiotemporal characteristics of seismicity based  
361 on precise earthquake locations: *Journal of Geophysical Research*, v. 117, B07304,  
362 <https://doi.org/10.1029/2011JB008966>, 2012.



- 363 Çemen, I., Göncüoğlu, M.C., and Dirik, K.: Structural evolution of the Tuz Gölü basin in central  
364 Anatolia, Turkey: *Journal of Geology*, v. 107, p. 693–706, <https://doi.org/10.1086/314379>, 1999.
- 366 Çubuk Y, Yolsal-Çevikbilen S, Taymaz, T.: Source parameters of the 20052008 Balırsirapinar  
367 (central Turkey) earthquakes: Implications for the internal deformation of the Anatolian  
368 plate. *Tectonophysics* 635(Supplement C) :125 – 153, 2014.
- 369 Delph, J.R., Biryol, C.B., Beck, S.L., Zandt, G., and Ward, K.M.: Shear wave velocity structure  
370 of the Anatolian plate: Anomalous slow crust in southwestern Turkey: *Geophysical*  
371 *Journal International*, v. 202, p. 261–276, 2015.
- 372 Eken, T., Mayeda, K., Hofstetter, A., Gök, R., Orgülü, G. and Turkelli, N.: An application of the  
373 coda methodology for moment-rate spectra using broadband stations in Turkey.  
374 *Geophys. Res. Lett.*, 31, L11609, 2004.
- 375 Eulenfeld, T. and Wegler, U.: Measurement of intrinsic and scattering attenuation of shear  
376 waves in two sedimentary basins and comparison to crystalline sites in Germany,  
377 *Geophys J Int.*, 205(2):744-757, 2016.
- 378 Eulenfeld, T. and Wegler, U.: Crustal intrinsic and scattering attenuation of high-frequency  
379 shear waves in the contiguous United States. *J Geophys., Res*, 122, 2017.
- 380 Favreau, P., and Archuleta, R.J.: Direct seismic energy modelling and application to the 1979  
381 Imperial Valley earthquake, *Geophys. Res. Lett.*, 30, 1198, 2003.
- 382 Fichtner, A., Saygin, E., Taymaz, T., Cupillard, P., Capdeville, Y., and Trampert, J.: The deep  
383 structure of the North Anatolian Fault Zone, *Earth Planet. Sc. Lett.*, 373, 109–117,  
384 2013a.
- 385 Fichtner, A., Trampert, J., Cupillard, P., Saygin, E., Taymaz, T., Capdeville, Y., and Villasenor,  
386 A.: Multiscale full waveform inversion, *Geophys. J. Int.*, 194, 534–556,  
387 [doi:10.1093/gji/ggt118](https://doi.org/10.1093/gji/ggt118), 2013b.



- 388 Gaebler, P.J., Eulenfeld, T. & Wegler, U.: Seismic scattering and absorption parameters in the  
389 W-Bohemia/Vogtland region from elastic and acoustic radiative transfer theory,  
390 Geophys. J. Int., 203(3), 1471–1481, 2015.
- 391 Gaebler, P.J., Eken, T., Bektaş, H.Ö., Eulenfeld, T., Wegler, U., Taymaz, T.: Imaging of Shear  
392 Wave Attenuation Along the Central Part of the North Anatolian Fault Zone, Turkey,  
393 submitted to the Journal of Seismology, 2018.
- 394 Gök, R., Kaviani, A., Matzel, E. M., Pasyanos, M. E., Mayeda, K., Yetirmishli, G., El-  
395 Hussain, I., Al-Amri, A., Al-Jeri, F., Godoladze, T., Kalafat, D., Sandvol, E. A., and  
396 Walter, W.R.: Moment Magnitudes of Local/Regional Events from 1D Coda  
397 Calibrations in the Broader Middle East Region. Bull Seismol Soc Am., 106(5):1926-  
398 1938, 2016.
- 399 Gusev, A.A. & Abubakirov, I.R.: Simulated envelopes of non-isotropically scattered body  
400 waves as compared to observed ones: another manifestation of fractal heterogeneity,  
401 Geophys. J. Int., 127(1), 49–60, 1996.
- 402 Hanks, T.C. and Kanamori, H.: A moment magnitude scale, J. Geophys., Res., 84, 2348–  
403 2350, 1979.
- 404 Higgins, M., Schoenbohm, L.M., Brocard, G., Kaymakci, N., Gosse, J.C., and Cosca, M.A.:  
405 New kinematic and geochronologic evidence for the Quaternary evolution of the  
406 Central Anatolian fault zone (CAFZ), Tectonics, v. 34, pages, 2118- 2141, 2015.
- 407 Izgi, G., Eken, T., Gaebler, P., and Taymaz, T.: Frequency-Dependent Shear Wave  
408 Attenuation Along the Western Part of the North Anatolian Fault Zone, Geophysical  
409 Research Abstracts, Vol. 20, EGU2018-629-2, 2018.
- 410 Kaymakci, N. Inceöz, M. Ertepinar, P.: 3D architecture and Neogene evolution of the Malatya  
411 Basin: inferences for the kinematics of the Malatya and Ovacik Fault Zones. Turkish  
412 Journal of Earth Sciences, 15, 123-154, 2006.



- 413 Kwiatek, G., Plenkers, K. & Dresen, G.: 2011. Source parameters of pico-seismicity recorded  
414 at Mponeng Deep Gold Mine, South Africa: implications for scaling relations, Bull.  
415 seism. Soc. Am., 101(6), 2592–2608, 2011.
- 416 Malagnini, L., Mayeda, K., Akinci, A., and Bragato, P. L.: Estimating absolute site effects,  
417 Bull. Seismol. Soc. Am. 94, no. 4, 1343–1352, 2004.
- 418 Mayeda, K., and Walter, W.R.: Moment, energy, stress drop, and source spectra of western  
419 United States earthquakes from regional coda envelopes, J. Geophys. Res. 101,  
420 11,195–11,208, 1996.
- 421 Mayeda, K., Hofstetter, A., O’Boyle, J.L., and Walter, W.R.: Stable and transportable  
422 regional magnitudes based on coda-derived moment-rate spectra, Bull. Seismol. Soc.  
423 Am. 93, 224–239: 2003.
- 424 Morasca, P., Mayeda, K., Malagnini, L. and Walter, W.R.: Coda and direct-wave attenuation  
425 tomography in northern Italy, Bull Seismol Soc Am., v. 98, pages, 1936-1946, 2004.
- 426 Morasca, P., Mayeda, K., Gök, R., Phillips, W.S., and Malagnini, L.: Coda-derived source  
427 spectra, moment magnitudes and energy-moment scaling in the western Alps,  
428 Geophys. J. Int., 160, 263–275, 2008.
- 429 Paasschens, J.: Solution of the time-dependent Boltzmann equation, Phys. Rev. E, 56(1),  
430 1135–1141, 1997.
- 431 Portner, D.E., Delph, J.R., Biryol, C.B., Beck, S.L., Zandt, G., Özacar, A.A., Sandvol, E., and  
432 Türkelli, N.: Subduction termination through progressive slab deformation across  
433 Eastern Mediterranean subduction zones from updated P-wave tomography beneath  
434 Anatolia, Geosphere, 14(3): 907-925, 2018.
- 435 Przybilla, J. and Korn, M.: Monte Carlo simulation of radiative energy transfer in continuous  
436 elastic random mediathree-component envelopes and numerical validation. Geophys J  
437 Int , 173(2):566-576, 2008.



- 438 Rautian, T.G. & Khalturin, V.I.: The use of the coda for determination of the earthquake  
439 source spectrum, *Bull. Seism. Soc. Am.*, 68(4), 923–948, 1978.
- 440 Sato, H. and Fehler, M.C.: *Seismic Wave Propagation and Scattering in the Heterogeneous*  
441 *Earth*, Springer-Verlag, New York, 1998.
- 442 Sato, H., Fehler, M.C. & Maeda, T. *Seismic Wave Propagation, and Scattering in the*  
443 *Heterogeneous Earth*, 2nd edn, Springer: 2012.
- 444 Sens-Schönfelder, C. and Wegler, U.: Radiative transfer theory for estimation of the seismic  
445 moment. *Geophys J Int*, 167(3):1363-1372.
- 446 Şengör, A.M.C., Tüysüz, O., İmren, C., Sakiñç, M., Eyidoğan, H., Görür, N., Le Pichon, X.,  
447 and Rangin, C.: The North Anatolian fault: A new look: *Annual Review of Earth and*  
448 *Planetary Sciences*, v. 33, p. 37–112, 2005.
- 449 Taymaz, T., Jackson, J., Westaway, R.: Earthquake mechanisms in the Hellenic Trench near  
450 Crete. *Geophys. J. Int.* 102, 695–731, 1990.
- 451 Taymaz, T., Westaway, R., Reilinger, R.: Active faulting and crustal deformation in the  
452 eastern Mediterranean Region. *Spec. Issue Tectonophys.* 391 (1-4), 1–9. [http://](http://dx.doi.org/10.1016/j.tecto.2004.07.005)  
453 [dx.doi.org/10.1016/j.tecto.2004.07.005](http://dx.doi.org/10.1016/j.tecto.2004.07.005), 2004.
- 454 Yoo, S.-H., Rhie, J., Choi, H.-S., and Mayeda, K.: Coda-derived source parameters of  
455 earthquakes and their scaling relationships in the Korean Peninsula, *Bull. Seismol.*  
456 *Soc. Am.*, 101, 2388–2398, 2011.
- 457 Wu, R. and Aki, K.: The fractal nature of the inhomogeneities in the lithosphere evidenced  
458 from seismic wave scattering, *Pure appl. Geophys.*, 123(6), 805–818, 1985.
- 459 Zeng, Y., Su, F. and Aki, K.: Scattering wave energy propagation in a random isotropic  
460 scattering medium: 1. Theory, *J. Geophys. Res.*, 96(B1), 607–619, 1991.

461

462

463 *Figure Captions*

464 Figure 1. Major tectonic features of Turkey and its adjacent. The plate boundary data used  
465 here is taken from Bird (2003). Subduction zones are black, continental transform faults are  
466 red, continental rift boundaries are green, and spreading ridges boundaries are yellow. NAFZ,  
467 EAFZ, and DSFZ are the North Anatolian Fault, East Anatolian Fault, and the Dead Sea fault,  
468 respectively.

469

470 Figure 2. Epicentral distribution of all local events selected from the study area in the KOERI  
471 catalogue. Gray circles represent earthquakes with poor quality that are not considered for the  
472 current study while black indicates the location of local events with good quality. Red circles  
473 among these events are 487 events used in coda wave inversion since they are successful at  
474 passing quality criteria of further pre-processing procedure.

475

476 Figure 3. An example from the inversion procedure explained in chapter 3. Here coda  
477 envelope fitting optimization is performed on band-pass filtered (8-16Hz) digital recordings  
478 of an earthquake (2014 April 09,  $M_w$ -coda3.2) extracted for 7 seismic stations that operated  
479 within the CD-CAT array. Large panel at the lower left-hand side displays the error function  $\epsilon$   
480 as a function of  $g_0$ . Thick blue cross here represent the optimal value of  $g = g_0$ . Other small  
481 panels at upper and right-hand side show the least- squares solution of the weighted linear  
482 equation system for the first 6 guesses and optimal guess for  $g_0$ . There dots and gray curves  
483 indicate the ratio between energy ( $E^{obs}$ ) and the Green's function ( $G$ ) obtained for direct S-  
484 waves and observed envelopes at various stations, respectively. Please notice that during this  
485 optimization process envelopes are corrected for the obtained site corrections  $R_i$ . The slope of  
486 linear curve at each small panel yields  $-b$  and while its intercept  $W$  are the intrinsic





487 attenuation and source related terms at the right-hand side of equation 4 part of the right-hand  
488 side of the equation system.

489

490 Figure 4. a) Results of the inversion of the 2014-April-09,  $M_w$ -coda3.2 earthquake: Sample  
491 fits between observed and calculated energy densities in the frequency band 0.5–1.0 Hz are  
492 given for 6 different stations (see upper right corner for event ID, station name, and distance  
493 to hypocenter). Note that light blue curves represent observed envelope. Smoothed observed  
494 calculated envelopes in each panel are presented by blue and red curves, respectively. Blue  
495 and red dots exhibit location of the average value for observed and calculated envelopes  
496 within the S-wave window, respectively. b) The same as in (a) obtained in the frequency band  
497 4.0–8.0 Hz.

498

499 Figure 5. All individual observed (black squares) and predicted (gray curve) source  
500 displacement spectra observed at 72 stations from 487 local earthquakes in central Anatolia.

501

502 Figure 6: Scatter plot between local magnitudes ( $M_L$ ) of analyzed events with coda waves-  
503 derived magnitudes ( $M_w$ -coda) of the same events. The outcome of a linear regression  
504 analysis yielded an empirical formula (e.g. Eq. 9) to identify the overall agreement represented  
505 by gray straight line. Yellow and red dashed lines indicate upper and lower limit of linearly  
506 fitting to that scatter.

507

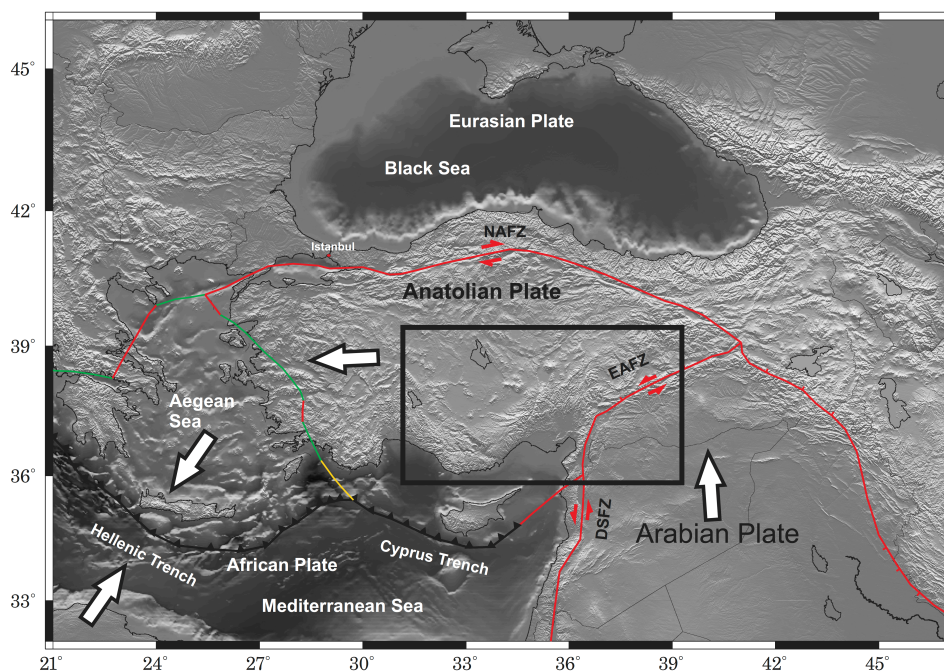
508 Figure 7: Same scatter plot displayed in Fig. 6 color coded by estimated high-frequency fall-  
509 off parameter for each inverted event.

510

511



512  
513  
514

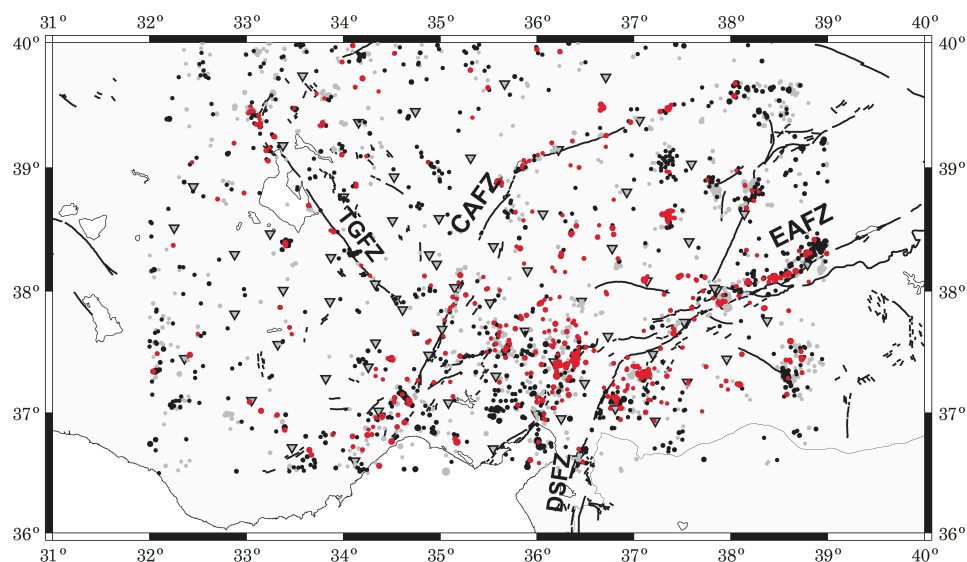


515  
516  
517  
518  
519  
520  
521  
522  
523  
524  
525  
526

Figure 1.



527



528

529 Figure 2.

530

531

532

533

534

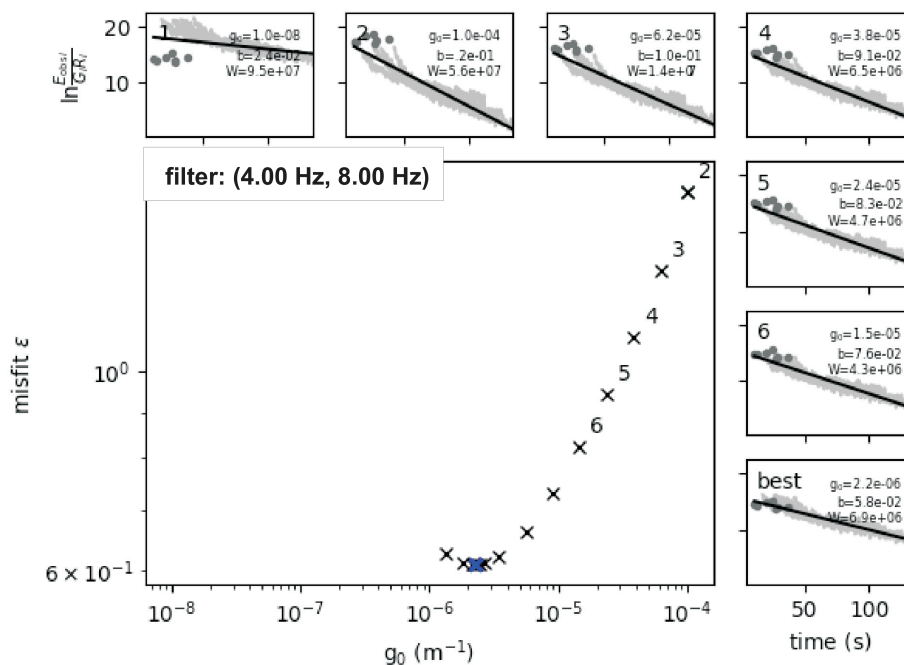
535

536

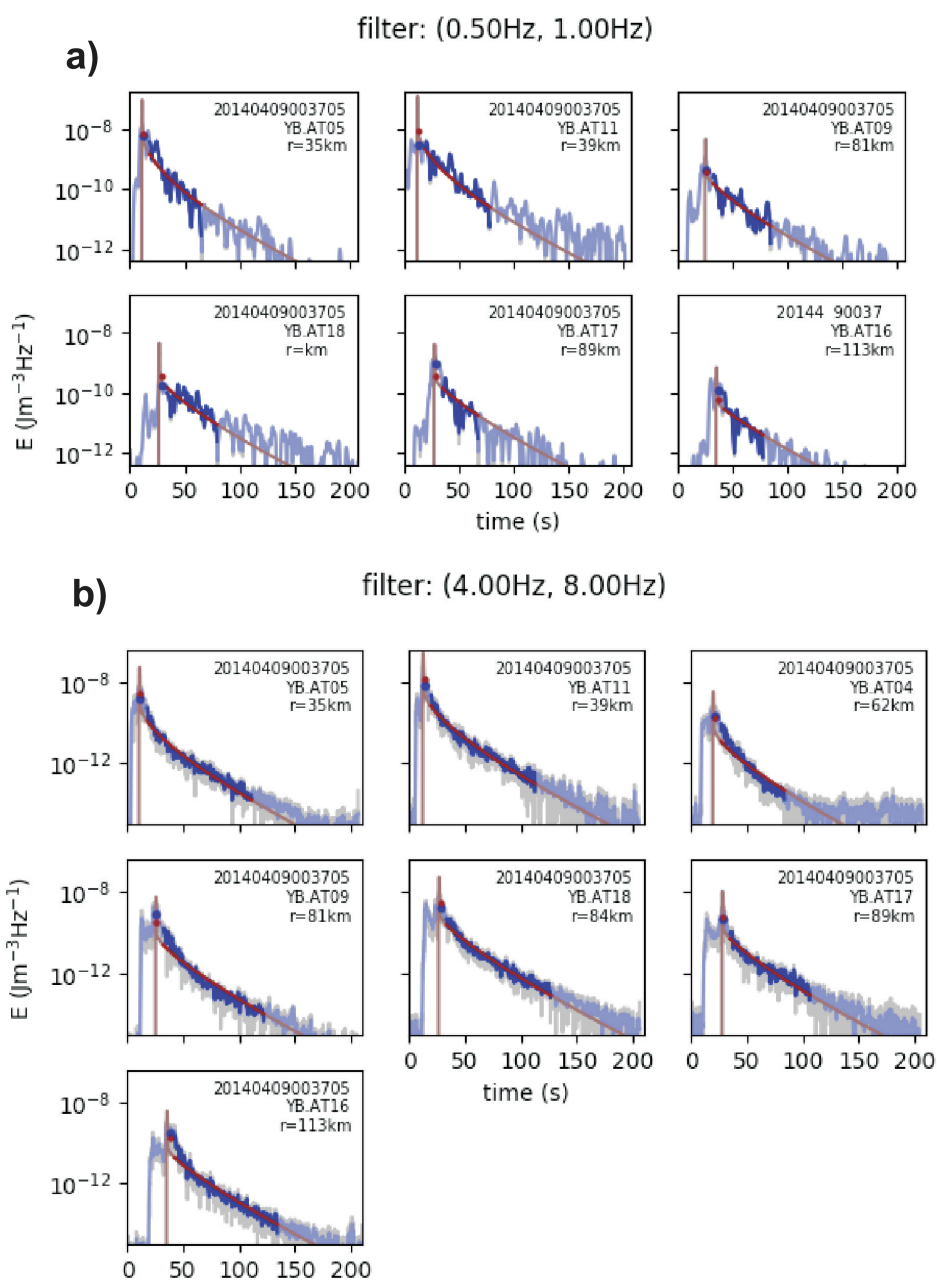
537

538

539



540  
 541  
 542  
 543 Figure 3.  
 544



545

546

547

548

549

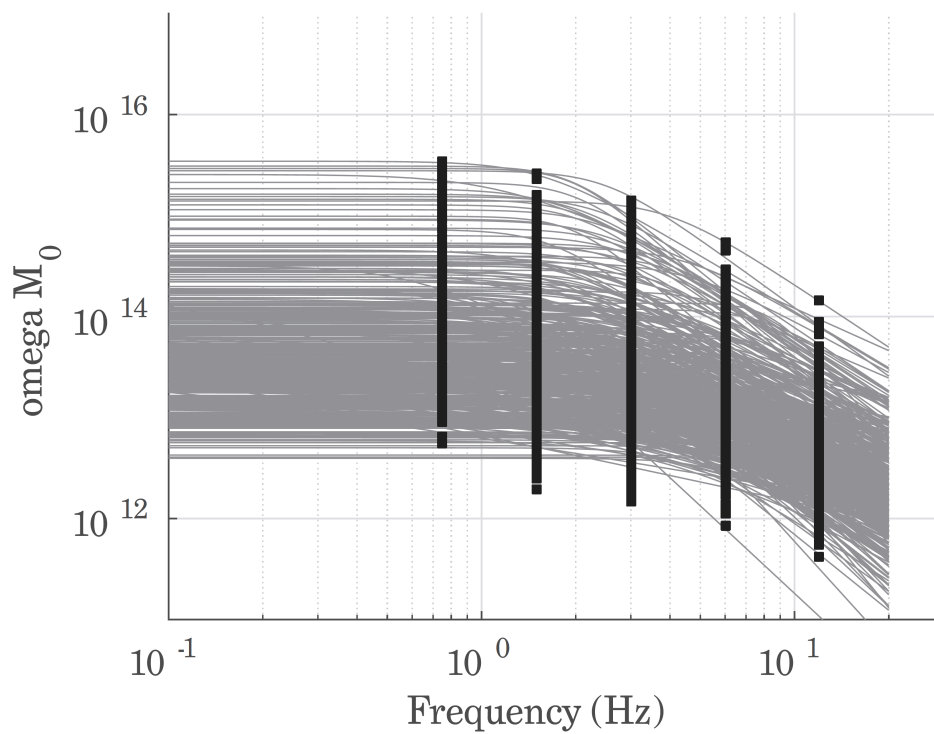
550

551

Figure 4.



552  
553  
554  
555  
556

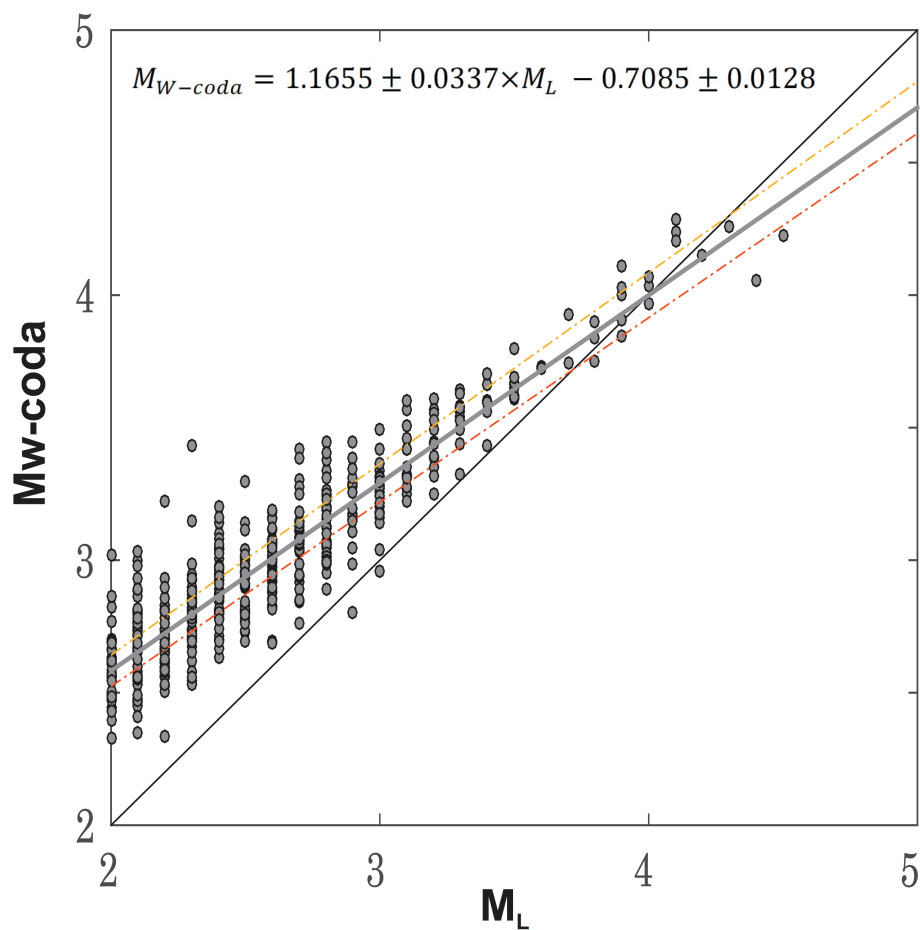


557  
558  
559  
560  
561  
562  
563  
564  
565  
566  
567  
568  
569  
570  
571  
572  
573  
574  
575  
576  
577

Figure 5.



578  
579  
580  
581  
582  
583

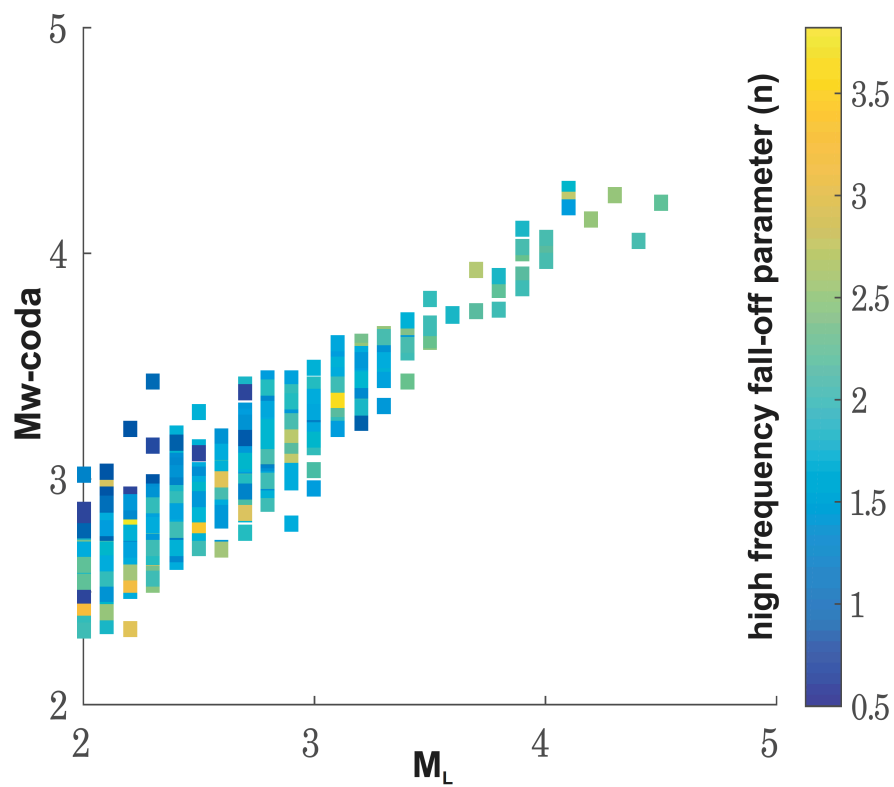


584  
585  
586  
587  
588  
589  
590  
591  
592  
593  
594  
595  
596  
597

Figure 6.



598  
599



600  
601  
602  
603

Figure 7.